Future Technology
Open Access Journal
ISSN 2832-0379

May 2024| Volume 03 | Issue 02 | Pages 01-10

Journal homepage: https://fupubco.com/futech

https://doi.org/10.55670/fpll.futech.3.2.1

Future Publishing LLC

Article

Modeling and sensitivity analysis of a supersonic inductive Magnetohydrodynamic (MHD) generator

Hossein Yousefi, Mohammad Mahmoudi, Mohammad Hasan Ghodusinejad*

Department of Renewable Energies and Environment, Faculty of New Sciences and Technologies, University of Tehran, Tehran, Iran

ARTICLE INFO

Article history:
Received 10 July 2023
Received in revised form
12 August 2023
Accepted 20 August 2023

Keywords:
Supersonic inductive MHD generator,
Direct energy conversion, High-temperature flow, High Mach number flow, Multiphysics numerical modeling

*Corresponding author
Email address:
mh.ghodusi@ut.ac.ir

DOI: 10.55670/fpll.futech.3.2.1

ABSTRACT

This study presents the supersonic inductive Magnetohydrodynamic (SIMHD) generator and simulates its model through the use of COSMOL Multiphysics. This generator, as an inductive MHD generator, is suggested to address the problems associated with the conventional MHD generator. Since the proposed generator does not require a moving part to convert thermal energy to electrical energy, it is categorized as a direct energy convertor. The SIMHD generator consists of a converging-diverging duct and is divided into two sections at the diverging part by means of a diaphragm. Both of these sections are diverging, which makes it possible to obtain a high Mach number. In this regard, the performance of the SIMHD generator is studied by its mathematical modeling and numerical simulation using the finite element method. In addition, a sensitivity analysis is carried out on the design parameters. The results indicate that the proposed SIMHD duct design will increase the speed from 160 to 1300 m/s, and decrease the temperature from 2100 to 1300 K. Moreover, considering a charge generation equation, the produced power for the resistive load 50 Ω equals 25.3 kW. This generator also has the potential to be used in scramjets and ramjets.

1. Introduction

Since the beginning of the twentieth century, the applicability of Magnetohydrodynamic (MHD) Generators for the replacement of gas turbine-based energy conversion has been widely investigated [1-8]. Without the utilization of any mechanically moving part, the MHD power generation can convert thermal energy into electrical energy, and so this energy conversion system has attracted much attention [9-12]. These generators are not efficient unless the level of the charge concentration in the gas is increased to the conductivity level [7, 13, 14]. To achieve this end, the gas is highly heated and seeded with ionizing elements like alkaline metals [6, 9, 13, 15]. One of the main problems of these MHD generators is the high temperature that is required for ionizing the gas to operate [2, 9, 15]. Two other problems are also associated with these generators, which must be taken into consideration: (1) they require a high magnetic field (about 5 T) for which superconducting windings are needed [16], (2) the high-temperature plasma can destroy the electrodes which are in contact with it [16, 17]. To overcome these shortcomings, references [18-21] introduced a type of MHD generator. This model of MHD generator requires no external magnetic field as its conversion process proceeds on the basis of the induction which a non-static current generates. In addition, since an electric discharge is responsible for the production of charge carriers, their concentration is not influenced by the temperature. Consequently, no electrode necessarily undergoes deterioration because of the magnetic coupling of the plasma and the electric load. The inductive gas-fed generator of this type of MHD generator, in addition to observing all the merits of the conventional MHD generator (e.g., the static conversion of energy and working with high temperatures), makes it possible to obviate the aforementioned shortcomings. In this model, an external electric field and a diaphragm that divides the field current into two parts split the charge carriers preceded by a set of electric discharges that ionizes the operating fluid. The unsteady nature of the electrical current, which results from the drag movement of charge carriers, leads to the induction of an electromotive force, a toroidal coil that is put around the pipes. To increase the gas speed and decrease the distance between the electrodes, which results in a lower potential difference, a converging-diverging duct was utilized in this study. To identify whether a desirable level of energy can be transmitted to the electric load, some studies which involve this process have been carried out [18-21]. In this paper, the Finite Element Analysis (FEM) has been utilized for the investigation of Supersonic Inductive MHD

generators. In addition, to make the simultaneous consideration of both dynamic and electromagnetic dimensions, a multi-physics approach has been employed. In this regard, the physical phenomenon of the problem is described in Section 2. The numerical model is presented in Section 3. The model results are discussed in Section 4. The conclusion of the study is presented in Section 5.

2. Physical phenomena description

Like an inductive MHD generator, the supersonic inductive MHD (SIMHD) generator can be categorized as direct energy conversion since it directly converts the energy from fossil fuel into electricity. Like all the other direct energy conversion processes, this model of generators is capable of converting thermal energy into electricity without using any moving parts. In comparison with the conventional MHD generator, there is no need for an external magnetic field in this model. While due to the principle of inductivity, the conversion of energy is still possible. This generator operates based on simple principles. Initially, a high-speed gas enters the duct. Here, through a pulsating electric discharge, the gas is ionized. An external electric field is utilized to split the charges of the different signs. A force $\vec{F} = Q\vec{E}$, which is parallel to the direction of $\vec{E}$ and separates the charges with different signs in the direction of the movement of the fluid, is produced on each charge Q of the fluid by the movement of the ionized fluid in an electric field $\vec{E}$. The flow is divided into two charge currents by a diaphragm, one with an excess of positive charge and the other with an excess of negative charge. An electromotive force is induced in toroidal coils put around a highly permeable magnetic core which is placed in the cavity and around the duct by the generated current. Figure 1 displays a representational scheme of the SIMHD generator, which consists of three main sections. The first section is responsible for the ionization of the inlet fluid. In the second section, the charges are separated. Finally, in the third section, the energy is transmitted to the electric load. There are different methods that can be utilized for the ionization of the fluid. In this study, it is assumed that the electrodes, which are powered by a high-voltage generator to produce a pulsating electric discharge, ionize the fluid.

To reach the appropriate electric current, there is a need for the generation of an adequate number of charge carriers during the discharge process. The electrode must be located in the initial part of the duct, connected to the pulse generator, which produces a high voltage. It also needs to be in contact with the ionized fluid. It must also be noted that the pulse generator needs to be appropriately set in order to select the discharge generation optimal parameters. A DC high-voltage generator externally powers the two plates of a capacitor which are placed in the second section of the generator to separate the charges. To avoid the blockage of the charge carriers inside the device, the external electric field should be well-calibrated and fine-tuned. That is, the capacitor plates must be powered by a voltage that is sufficiently high to separate the positive and negative charges and not so high to block the charges in the internal side of the apparatus. Finally, two currents of fluid, one with an excess of positive charge and one with an excess of negative charge, enter the third section of the apparatus. The diaphragm is placed in the third section of the generator, and as soon as the fluid currents enter the section, they are divided into two asymmetric flows, which are electrically unbalanced. Therefore, a ring of electric current is created around the diaphragm (Figure 1). In this section, some of the energy of the fluid is carried to the external load, and it is here that the energy is converted. The ring of the generated electric current varies with time, and as a result, an electromotive force is induced in the toroidal coil around a core that has a high magnetic permeability. This core is around the generator in the cavity. The charges are then neutralized as the two currents combine downstream of the third section. It can be observed that an external electric field separates the negative and positive charges, and there is no need for the generation of any external magnetic field. What makes energy conversion possible is the existence of the inductive process. As an electric discharge produces the electric charge, the gas can be ionized at low temperatures if the pulsing voltage is sufficiently high, and since there is the magnetic coupling of the plasma and the electric load, no electrode will be destroyed.

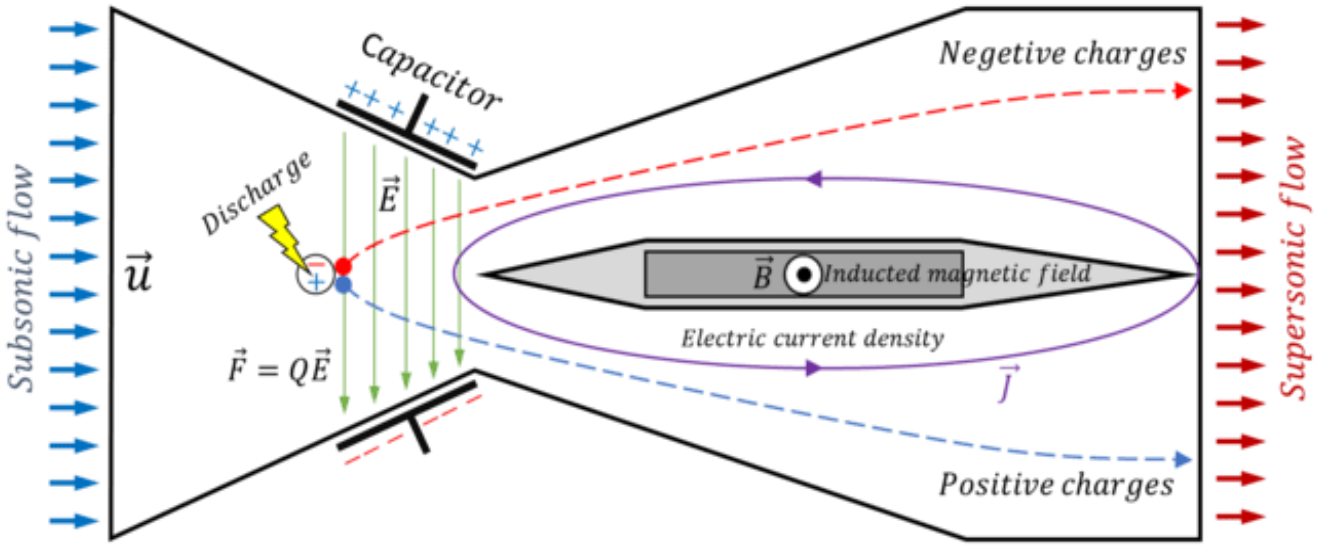

Figure 1. The SIMHD generator functional scheme

3. Model description

The system of coupled (nonlinear) equations is used to describe the mathematical time-dependent model of plasma flow in an electric field. This system is composed of Poisson's equation for electric potential, the Navier-Stokes equation and the conservation energy equation for fluid, and the charge transport equation for electric charge density.

3.1 Electrostatic

The Poisson's equation which results in the electric potential V is as follows:

$$\nabla^2 V = -\frac{q}{\varepsilon_0} \quad (1)$$

where, $q\left(SI\ unit: {}^{C}/_{m^3}\right)$ is the space charge density , and ε_0 is the dielectric permittivity of the free space.

The electric field intensity $\vec{E}$ defines the electric potential, as in Equation (2):

$$\vec{E} = -\nabla V \quad (2)$$

3.2 Fluid dynamic

The Navier-Stokes equations depict that part of the problem which is related to the fluid dynamic of the gas flow with the steady state turbulence. Turbulence modeling has a crucial role to play in the calculations of hypersonic flows. A turbulence model must always be included in the flow modeling since turbulent flows exist in many hypersonic applications. According to the one differential equation, Balswin and Barth have presented a new class of turbulence models. The most recent development of these models is represented by the Spalart-Allmaras $(S-A)$ model. The classical Prandtl approach in which the turbulent kinetic energy equation is used to arrive at the model equation ,is not adhered to in this new class. To create the equation in the $S-A$ model, Galilean invariance, selective dependence on the molecular viscosity, dimensional analysis empiricism and argumentation are employed. But the equation in Baldwin-Barth model is obtained from $k-\epsilon$ model [22, 23]. The velocity, pressure, and temperature fields are obtained by the $S-A$ model all the way down to the wall. That is why this model is referred to as a Low-Reynolds number model. Different applications of the $S-A$ model has proven to be successful [24]. To be solved, this model only requires one transport equation of the quantity $\tilde{\nu}\ (or\ \nu^t)$, which equals the eddy viscosity ν_t far away from the walls. The reason behind the construction of this transport equation has been the empirical reproduction of the flows with great intricacy [25].

$$\rho(\vec{u}\cdot\nabla)\vec{u} = \nabla\cdot\left[-p\vec{I} + (\mu+\mu_T)(\nabla\vec{u} + (\nabla\vec{u})^T) - \frac{2}{3}(\mu + \mu_T)(\nabla\cdot\vec{u})\vec{I}\right] + \vec{F} \quad (3)$$

where, $\vec{F}\left(SI\ unit: {}^{N}/_{m^3}\right)$ is the body force and is obtained by the following equation:

$$\vec{F} = \vec{J}\times\vec{B} - q\nabla V \quad (4)$$

The Navier-Stokes equation does not take the body forces into equation. With the left circuit open, the magnetic field reaction is near zero ($\vec{J}\times\vec{B} = 0$) in the case investigated. In addition, the body force $(-q\nabla V)$ can be ignored since the concentration of charge q in the fluid is very low. The relationship between the shear rate and the shear stresses in a fluid is described by the dynamic viscosity $\mu(SI\ unit: Pa\cdot s)$. The Sutherland's law is used to compute the coefficients of viscosity [25, 26]. The relationship between the ideal fluid's dynamic viscosity and its total temperature is described by this law based on:

$$\mu = \mu_{ref}\left(\frac{T}{T_{\mu,ref}}\right)^{3/2}\frac{T_{\mu,ref}+S_\mu}{T+S_\mu} \quad (5)$$

where μ_{ref} is the dynamic viscosity at reference temperature, $T_{\mu,ref}\ (SI\ unit: K)$ is the reference temperature, and $S_\mu\ (SI\ unit: K)$ is the Sutherland constant. Table 1 presents Sutherland's law parameters for dynamic viscosity for different gases. In this study, the properties of the air were utilized to solve the equations of the fluid dynamic.

Table 1. Sutherland's law parameters for dynamic viscosity (adopted from COMSOL software's documents)

Gas	μ_{ref} $(Pa\cdot s)$	$T_{\mu,ref}$ (K)	S_μ (K)
Air	1.716×10^{-5}	273	111
CO_2	1.370×10^{-5}	273	222
CO	1.657×10^{-5}	273	136
N_2	1.663×10^{-5}	273	107
O_2	1.919×10^{-5}	273	139
Steam	1.12×10^{-5}	350	1064

A partial differential equation is employed to calculate the eddy viscosity in the $S-A$ model. The parameters used in the S-A model is presented in Table 2. An intermediate variable ν^t is used to calculate the viscosity μ_T through the following equation.

$$\mu_T = \rho\nu^t f_{v1}(\chi) \quad (6)$$

where χ is the ratio determined by Equation (7):

$$\chi = \frac{\nu^t}{\nu} \quad (7)$$

and f_{v1} is a damping function calculated by Equation (8):

$$f_{v1} = \frac{\chi^3}{\chi^3+C_{v1}^3} \quad (8)$$

$$f_{v2} = 1 - \frac{\chi}{1+\chi f_{v1}} \quad (9)$$

$$(\vec{u}.\nabla)\nu^t = C_{b1}S^t\nu^t - C_{w1}f_w\left(\frac{\nu^t}{l_w}\right)^2 + \frac{1}{\sigma_{\tilde{\nu}}}\nabla\cdot\left((\nu+\nu^t)\nabla\nu^t\right) + \frac{C_{b2}}{\sigma_{\tilde{\nu}}}\nabla\nu^t\cdot\nabla\nu^t\ ,\nu^t = nutilde\ (\tilde{\nu}) \quad (10)$$

$$C_{w1} = \frac{C_{b1}}{\kappa_v^2} + \frac{1+C_{b2}}{\sigma_{\tilde{\nu}}} \quad (11)$$

Table 2. $S-A$ model's parameters (adopted from COMSOL software's documents)

Constant	Value
C_{b1}	0.1355
C_{b2}	0.622
C_{v1}	7.1
$\sigma_{\tilde{\nu}}$	$^2/_3$
C_{w2}	0.3
C_{w3}	2
κ_v	0.41
C_{Rot}	2

$$f_w = g\left(\frac{1+C_{w3}^6}{g^6+C_{w3}^6}\right)^{\frac{1}{6}} \quad (12)$$

$$g = r - C_{w2}(r^6 - r) \quad (13)$$

$$r = min(\frac{\nu^t}{S^t\kappa_v^2 l_w^2}, 10) \quad (14)$$

$$S^t = max\left(\Omega + C_{Rot}\, min(0, S-\Omega) + \frac{\nu^t}{\kappa_v^2 f_w^2} f_{v2}, 0.3\Omega\right) \quad (15)$$

$$\Omega = \sqrt{2\vec{\Omega}:\vec{\Omega}} \quad (16)$$

$$S = \sqrt{2\vec{S}:\vec{S}} \quad (17)$$

$$\vec{\Omega} = \frac{1}{2}(\nabla\vec{u} - (\nabla\vec{u})^T) \quad (18)$$

$$\vec{S} = \frac{1}{2}(\nabla\vec{u} + (\nabla\vec{u})^T) \quad (19)$$

The mass conservation is denoted by Equation (20):

$$\nabla\cdot(\rho\vec{u}) = 0 \quad (20)$$

The conservation of energy can also be described by Equation (21):

$$\rho C_p\vec{u}\cdot\nabla T = \nabla\cdot(k\nabla T) + Q_p \quad (21)$$

where $c_p(SI\ unit: {}^{J}/_{kg\cdot K})$ is the heat capacitance of the gas at constant pressure, and $Q_p(SI\ unit: {}^{W}/_{m^3})$ includes the heat sources, determined by Equation (22).

$$Q_p = \vec{J}\cdot\vec{B} \quad (22)$$

If the secondary circuit is open, there will be no transfer of energy. The heat sources can be neglected in the evaluation of electrohydrodynamic flow under these circumstances.
For thermal conductivity the Sutherland's law can also be formulated as follows [26]:

$$k = k_{ref}\left(\frac{T}{T_{\mu,ref}}\right)^{3/2}\frac{T_{k,ref}+S_k}{T+S_\mu} \quad (23)$$

where k_{ref} $(SI\ unit: {}^{W}/_{m\cdot K})$ is the thermal conductivity at reference temperature, $T_{k,ref}$ $(SI\ unit: K)$ is the reference temperature, and S_k $(SI\ unit: K)$ is the Sutherland constant which is mentioned in Table 3.

Table 3. Sutherland's law parameters for thermal conductivity (adopted from COMSOL software's document)

Gas	k_{ref} $\left(\frac{W}{m\cdot K}\right)$	$T_{k,ref}$ (K)	S_k (K)
Air	0.0241	273	194
CO_2	0.0146	273	1800
CO	0.0232	273	180
N_2	0.0242	273	150
O_2	0.0244	273	120
Steam	0.0181	300	2200

Finally, the equation of state is as follows:

$$p = \rho RT \quad (24)$$

3.3 Charge transport

Usually, the charge carriers which are present in the fluid are electrons and ions. The complex behavior of electrons in liquids or gases may be due to the collisions of ions with neutral molecules and other ions, photoionization, etc. the calculation of the velocity of the ions is a daunting task, and it has a great dependence on the local electric field [27, 28]. If the electronegative impurities or the molecules present in the fuel capture the electrons, then the only charge carriers in the fluid are the positive and negative ions. Under such circumstances, it is possible to regard these ions as spheres which are moving in a continuum and estimate their behavior based on the laws of an ideal gas of particles in the volume which is filled with the fluid [28]. Three factors affect the electric current in the drifting zone: conduction (motion of charges under electric field relative to entire flow), convection (transport of charges with flow), and diffusion [28, 29]. As a result, the current density $\vec{j}$ is calculated by Equation (25):

$$\vec{j} = \mu_E\vec{E}q + q\vec{u} - D\nabla q \quad (25)$$

Combining equation (2) with equation (25) leads to the following equation:

$$\vec{j} = q\vec{u} - D\nabla q - \mu_E q\nabla\vec{V} \quad (26)$$

where, μ_E $\left(SI\ unit: {}^{m^2}/_{V\cdot s}\right)$ is the mobility of the charge in an electric field, $\vec{u}$ is the flow's velocity vector, and D $\left(SI\ unit: {}^{m^2}/_{s}\right)$ is the diffusion coefficient of charges. By making a comparison between the peripheral particles' diffusion velocity and the velocity of these particles which results from their interaction with the distribution of the charge, the value of the diffusion coefficient is computed and by increasing this value, the effect of the charges repulsion has been accounted for. Taking into consideration the charge carriers' mobility, the diffusion would be $D = 2.1208\times 10^{-5}\ {}^{m^2}/_{s}$ instead of $D = 5\times 10^{-5}\ {}^{m^2}/_{s}$ which is the diffusion without charges interaction [19, 21, 29]. The equation for current density based on the current continuity condition is as follows:

$$\frac{\partial q}{\partial t} + \nabla\cdot\vec{j} = \begin{cases} \dot{q} & For\ charge\ generation\ region \\ 0 & For\ other\ regions \end{cases} \quad (27)$$

where, $\dot{q}$ $\left(SI\ unit: {}^{C}/_{m^3\cdot s}\right)$ is the charge generation rate.

$$\frac{\partial q}{\partial t} + \nabla\cdot\left(q\vec{u} - D\nabla q - \mu_E q\nabla\vec{V}\right) = \begin{cases} \dot{q} & For\ charge\ generation\ region \\ 0 & For\ other\ regions \end{cases} \quad (28)$$

3.4 Charge generation region

A gasifier or a combustion chamber feeds the duct with a gas [4, 30]. The literature indicates that the concentration of the charge carriers which results from the discharge is around $10^{14}\ {}^{n_e}/_{cm^3}$ [31, 32]. Assuming that in the process of discharge 10 cm^3 is engaged, the overall number of charges is approximately 2×10^{15}. $n_e\cdot e = 1.6\times 10^{-4}\ C$ and it will then be the charge of the same sign. A time varying flow of positive and negative charge carriers is injected to model the generation of the charges by the electrode. A space charge density q is used in the electric discharge region by applying the reaction rate parameter to the equation that follows:

$$R = \frac{\eta}{\sqrt{2\pi\delta^2}}\exp\left(\frac{-(t-t_1)^2}{2\delta^2} + \frac{-(t-t_2)^2}{2\delta^2} + \cdots + \frac{-(t-t_n)^2}{2\delta^2}\right) \quad (29)$$

where, R $\left(SI\ unit: {}^{C}/_{m^3\cdot s}\right)$ is the charge generation function, η and δ are the two parameters for adjusting this equation with charge density distribution, and $t_1, t_2, \ldots, t_n$ are the times when there is the maximum concentration of the

charges. In this context, Figure 2 displays the charge generation function and the time variation of charge density.

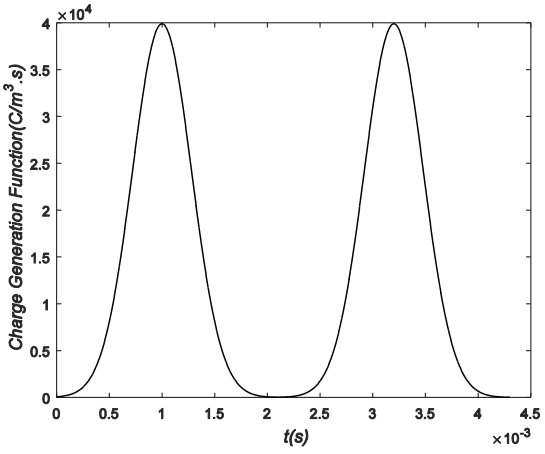

(a)

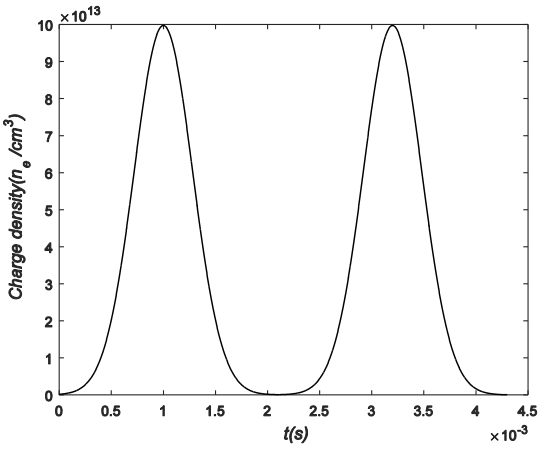

(b)

Figure 2. Time variation of (a) charge density function and (b) the charge generation function ($\eta = 30, \delta = 2.8 \times 10^{-4}$)

3.5 Energy conversion process

The functioning of the third section of the duct, where the physical process of energy conversion takes place and the electrical energy is transferred from the fluid electric current (primary winding) to the secondary winding by means of the inductive linkage, is the same as the functioning of a conventional transformer [33]. To calculate the force of the inductive electromotive force, an equivalent circuit in which the primary winding is equal to the current ring which flows along two parallel branches is assumed. It is also assumed that the secondary winding is comprised of a number of windings around two ferromagnetic rings which are put around the aforementioned branches (Figure 3). A varying electromotive force is induced in the secondary winding by a varying magnetic flux which is created by a varying current in the primary winding. An electric current flow in the secondary winding provided that a load is linked to it. In addition, an electric current will be transported to the electric load from the primary circuit through the transformer. An armature reaction is created by this electric current. This reaction reduces the speed of the charge carriers in the fluid and leads to the expansion of the gas. The magnetic flux $\phi(SI\ unit: Wb)$ is obtained by the following equation:

$$\phi = \frac{I(t)}{R_m} \tag{30}$$

where $R_m\left(SI\ unit: {}^{H}/_{m}\right)$ is the magnetic reluctance. The reluctance of a magnetically uniform magnetic circuit element can be computed as:

$$R_m = \frac{L}{\mu_m \cdot A} \tag{31}$$

where $l(SI\ unit: m)$ is the length of the element, $\mu_m\left(SI\ unit: {}^{N}/_{A^2}\right)$ is the permeability of the material and $A(SI\ unit: m^2)$ is the cross-section area of the circuit. The permeability of the material is determined using Equation (32):

$$\mu_m = \mu_{m,0} \cdot \mu_{m,r} \tag{32}$$

where $\mu_{m,0} = 4\pi \times 10^{-7}\ {}^{N}/_{A^2}$ is the permeability of free space, and $\mu_{m,r}$ is the ratio of the permeability of a specific medium to the permeability of free space that is assumed equal to $\mu_{m,r} = 4 \times 10^4$.

$$R_m = R_{m,c} + \frac{2R_{m,1}+R_{m,2}}{2} \tag{33}$$

$$\phi_c = \frac{2I}{2R_{m,1}+R_{m,2}+2R_{m,c}} \tag{34}$$

$$emf = N_s \frac{d\phi_c}{dt} \tag{35}$$

where N_s is the number of coils around the magnetic core.

$$Power = v_{rms}^2 \frac{R_{E,l}}{\left(R_{E,l}+R_{E,c}\right)^2} \tag{36}$$

where v_{rms} is the root mean square voltage and $R_{E,l}$ and $R_{E,c}$ are the external load resistive and the coil resistive respectively. If assumed that $R_{E,l} = R_{E,c}$ equation (36) will be:

$$Power = \frac{v_{rms}^2}{4R_E} \tag{37}$$

$$v_{rms} = \sqrt{\frac{1}{t_m}\int_0^{t_m} (emf)^2 dt} \tag{38}$$

where $t_m = t_{i+1} - t_i$ is the time between two consecutive electric discharges.

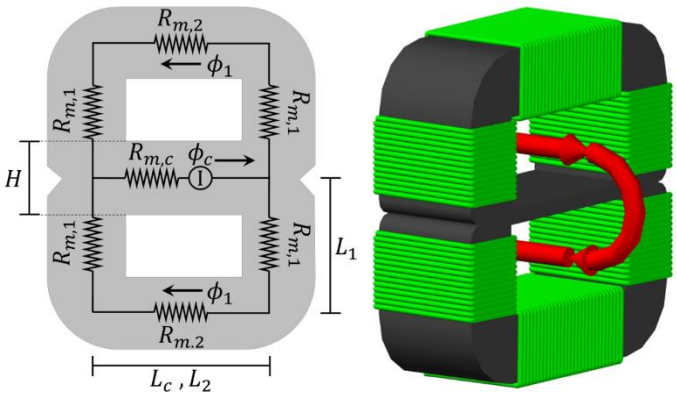

Figure 3. The equivalent magnetic circuit and 3D magnetic circuit scheme

4. Results and discussion

4.1 Modeling results

A 2D configuration model has been utilized in the present study. A converging-diverging shape is applied to the volume. The duct has a height of 110 mm, a length of 234 mm and a throat height of 40 mm. Figure 4 displays the boundaries, mesh, numerical simulation space, and subdomains of the model. The COMSOL Multiphysics 5.0 was employed to run the model by using the Finite Element Analysis (FEM). Three separate modules were used as follows:

- Electrostatics to solve the equations related to the electrostatic section;
- Fluid Flow (High Mach Number Flow (Turbulence Flow, Spalart – Allmaras)) to solve the Navier-Stoke's and energy equations;
- Transport of Diluted Species module that addresses the convection, diffusion, and migration in electric field aspects.

To solve the charge transport equation (Equation 28), the Diluted Species module was utilized. Since this module was used and the dependent variable of this module is the concentration of the components (c_i), where its unit is $\left({}^{mol}/_{m^3}\right)$, the concentration of the component is considered to be the same as the charge density of the components (positive ions and electrons) q_i. Following this assumption, $\left({}^{mol}/_{m^3}\right)$ can also be considered the same as $\left({}^{C}/_{m^3}\right)$.

A stationary study was carried out to solve the first two modules. The results of this study were utilized in a transient study to analyze the third module. To solve the equations of the charge transport in which transient interactive solvers are employed, the velocity and the electrical fields are computed and utilized as source terms. In the stationary study, the mesh in Figure 4 was used, which is appropriate for solving fluid equations. But in the transient study, the mesh in Figure 5 was used. The mesh depicted in Figure 4 is comprised of nearly 130000 elements which are more concentrated near the walls.

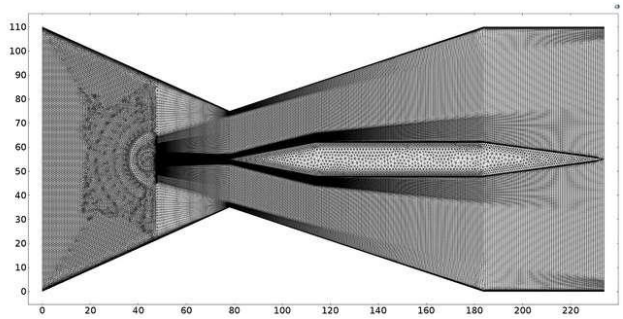

Figure 4. the boundaries, mesh, numerical simulation space, and subdomains of the model. (x and y axises are in mm)

An injection of charge carriers was done to simulate the electric discharge, which is shown by the circle. In this region, Equation 29 was inserted as the entry. The semi-circle around the discharge region was used as a virtual boundary to refine meshing. The following boundary conditions were applied to the numerical model. A no-slip function was employed in the inner walls of the duct in the fluid dynamic study. In the inlet section, the subsonic condition was applied to the inlet with a velocity of $M = 0.2$ and a total pressure of 5 atm. In the outlet section, the hybrid condition was applied to the fluid with a total pressure of 1 atm. A positive 30 kV DC voltage, which was constant, was applied to the external plates for electrostatic analysis. The mesh in Figure 5 consists of 110000 elements which are more concentrated where the charges move. This mesh was applied to the Transport of Diluted Species model where a zero diffusive flux condition is applied to all the boundaries but the outlet section in which convective flux diffusion is applied. Table 4 shows the modeling parameter values employed in FEM modeling.

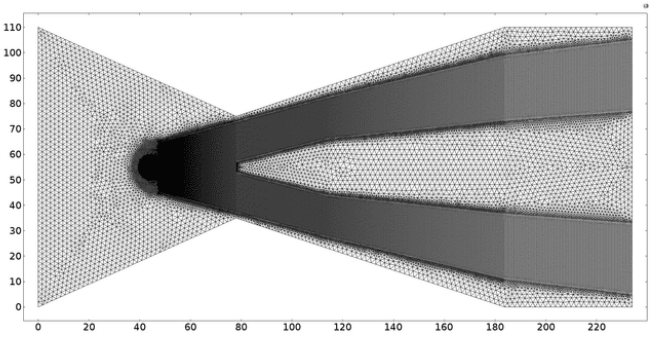

Figure 5. The mesh used in the charge transport equation

Table 4. The modeling parameter values used in FEM modeling

Parameter	Value
Relative dielectric permittivity of air, ε_r	1
Charge diffusion coefficient, D	$2.12 \times 10^{-4}\ {}^{m^2}/_{s}$
Ion mobility coefficient, μ_E	$1.8 \times 10^{-4}\ {}^{m^2}/_{V \cdot s}$
Density of the fluid at the inlet, ρ_{fluid}	$1.23\ {}^{kg}/_{m^3}$
Number of the coils around the magnetic core, N_s	8000
Time between two consecutive electric discharges, t_m	0.0023 s
Height of the cavity, H	8 mm
Mach number of fluid at the inlet, M_{in}	0.2
Inlet total temperature	2000 K
Inlet total pressure	5 atm
Outlet total pressure	1 atm
The difference in voltage between the capacitor plates	30 kV

As it is shown in Figure 6, the highest potential of the electric potential map is at the surface of the top capacitor armature, while at the bottom capacitor it has a decreasing magnitude. The magnitude of the gas velocity inside the channel is displayed in the velocity field map (Figure 7). As it can be seen in Figure 7, the oblique shocks can be observed in the regions where the velocity is higher than 1 Mach. These regions are shown specifically in Figure 8. The temperature and pressure fields are shown in Figure 9 and Figure 10, respectively. The oblique shocks can also be seen in these two figures. The movement of the charge carriers inside of the duct and the magnitude of the electric current density is shown at the $5 \times 10^{-4} th$, $1 \times 10^{-3} th$, and $2 \times 10^{-3} th$ seconds in Figure 11, Figure 12, and Figure 13, respectively. In Figure 14, the electric field lines, streamlines, and the direction of the charge

carriers' movement can be simultaneously observed. In this figure, the effect of fluid's movement and electric force on the movement of charge carriers is also shown.

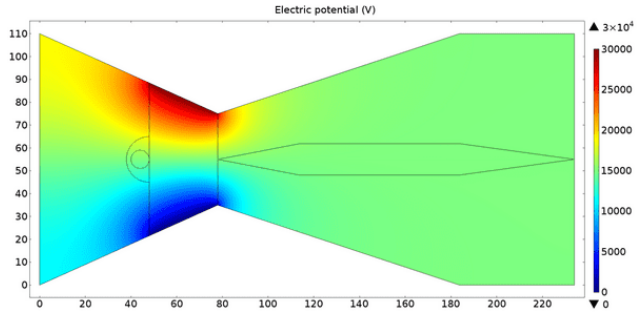

Figure 6. The distribution of electrical potential in the duct (V)

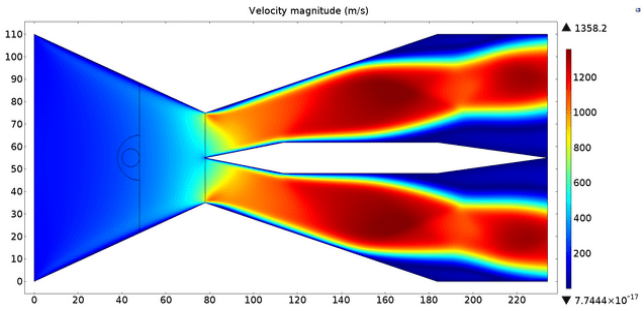

Figure 7. The velocity field in the duct (m/s)

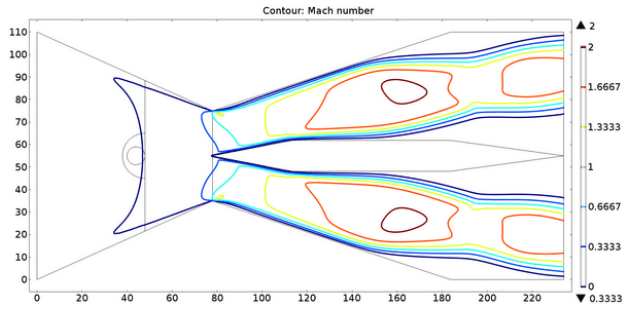

Figure 8. The mach number contour in the duct

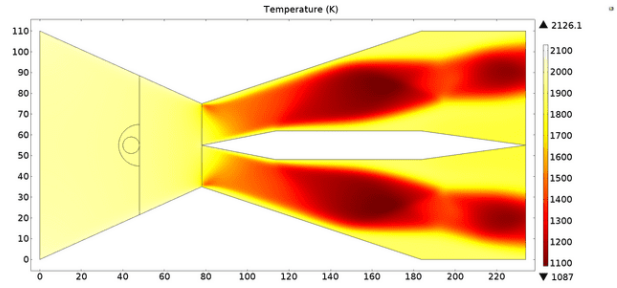

Figure 9. The fluid temperature field in the duct (K)

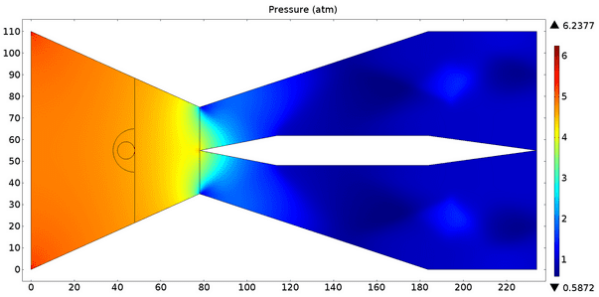

Figure 10. The pressure field in the (atm)

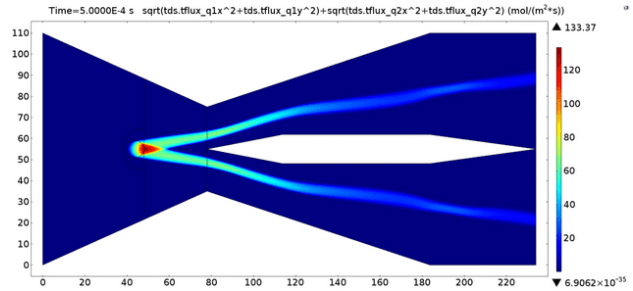

Figure 11. The electric current density $\left({}^{C}/_{m^2 \cdot s}\right)$ at 0.0005 s

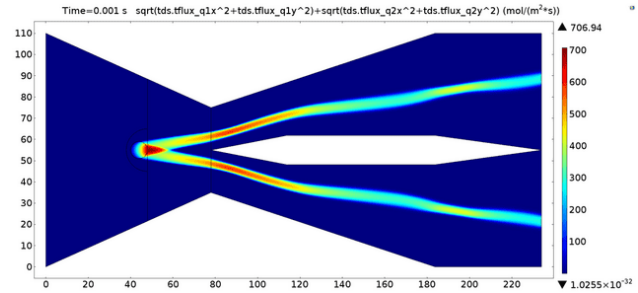

Figure 12. The electric current density $\left({}^{C}/_{m^2 \cdot s}\right)$ at 0.001 s

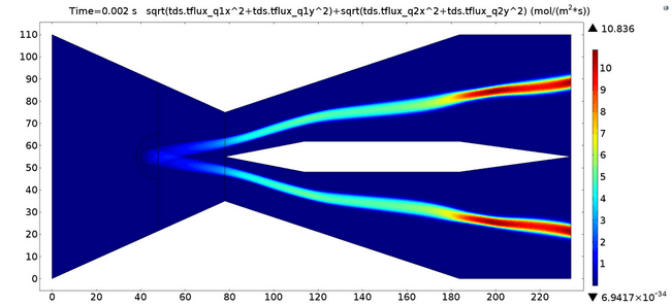

Figure 13. The electric current density $\left({}^{C}/_{m^2 \cdot s}\right)$ at 0.002 s

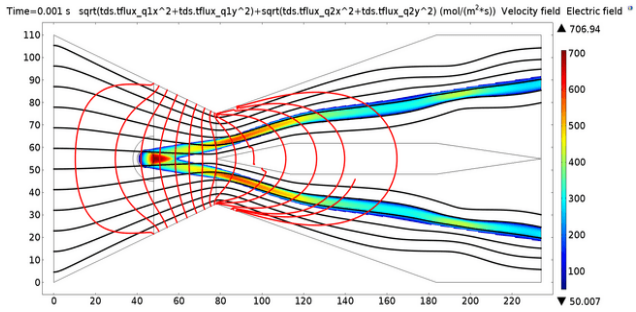

Figure 14. Electric field lines (red), streamlines (black), and the direction of the charge carriers' movement (the colored region, the unit of which is (C/(m²·s)))

An equivalent circuit, in which the motion of the electric charge in the fluid creates the primary winding and the 8000 coils, which are distributed over the branches of the magnetic circuit, constitute the secondary winding, is assumed so as to compute the inductive electromotive force. As shown in Figure 15, a voltage on the tops of the coil is arrived at by assuming the secondary winding is an open circuit. The assumed maximal power output has been computed by considering an adjusted load.

A theoretical maximum power near 25.3 kW is achieved by assuming Eq (36). By considering $R_{E,l} = R_{E,c}$, as mentioned before, the maximum power has been computed with the assumption of an adapted load. Under these assumptions, several factors reduce the functioning of the device, for example, if the external resistive load or the time interval between two successive electric discharges increase. The amount of power generated by changing the resistive load and the time interval between two successive electric discharges is shown in Figure 16. Here t_m represents the minimum time interval of interference between the two electric discharges. The decrease in the performance of the device is due to the increase of the external resistive load from 51 Ω to 800 Ω and the extension of the time interval between two electric discharges from t_m *to* 2.00 t_m is shown in Figure 16.

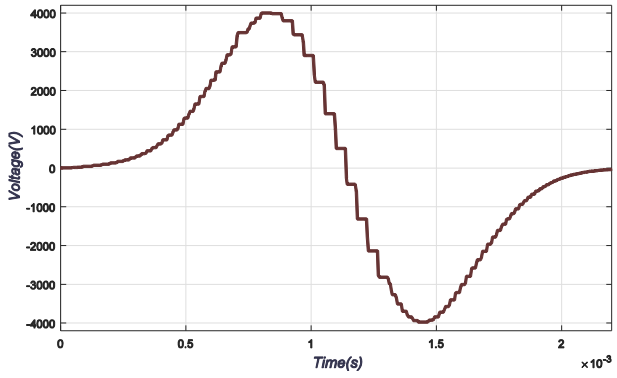

Figure 15. The inductive EMF on the heads of the open circuit

4.2 Sensitivity analysis

Taking some design parameters, such as the inlet temperature of the gas and the geometry of the generator into consideration, a sensitivity analysis was carried out. The functioning of the voltage of the coil's head and the theoretical maximum power load is calculated to see the effect of these parameters. The profile width of the diaphragm and the internal cavity of the diaphragm are the major dimension parameters that are taken into consideration. The working inlet temperatures have been changed at four points from 1800 to 2500 K to see how they affect the voltage of the head of the coil and the theoretical maximum power load. Figure 17 displays the voltage of the open circuit, which is obtained from changing the temperature of the working fluid and the height of the internal cavity of the diaphragm. As the temperature rises, the velocity of the charges increases, and as a result, the inducted gas voltage rises. However, it takes a shorter time period for the charge clouds to disperse; therefore, the charge clouds stay more concentrated. That section of the core which is inside the cavity becomes a bottleneck for the magnetic circuit and restrains the magnitude of the magnetic flux.

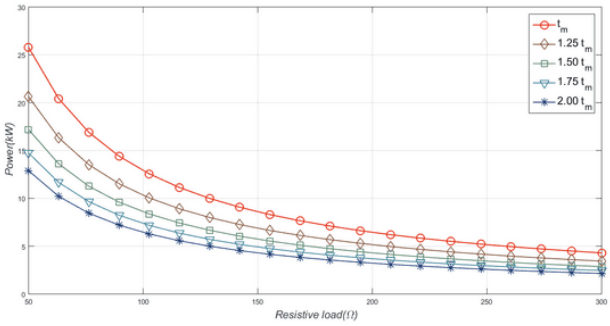

Figure 16. The trend of theoretical maximum generation power (kW) at different resistive loads (Ω) and time intervals

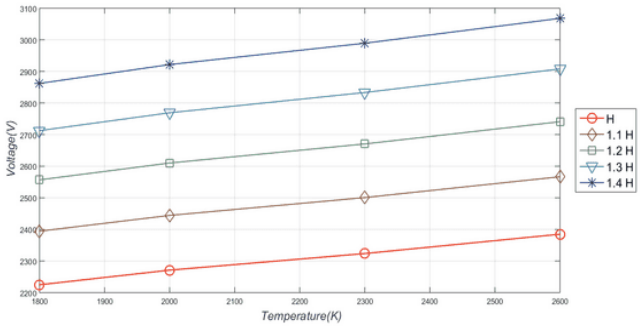

Figure 17. The voltage (V) of the open circuit obtained from varying the temperature (K) of the working fluid and the height of the internal cavity of the diaphragm

5. Conclusion

In the inductive MHD generator, there is no need for an external magnetic field, and it can perform at lower working temperatures in comparison with conventional MHD generators. The innovation of the SIMHD, in comparison with the inductive MHD generator, is that it uses a converging-diverging duct which increases the velocity, which in turn increases the voltage and generation power. This increased velocity will also result in a decrease in temperature in the second section of the duct, where the charge carriers are separated and cannot combine together. In the duct designed in this study, since the distance between the capacitor plates is less than that of the inductive MHD generator, a lower potential difference is required to separate the charge carriers. The Finite Element Analysis (FEM) and a multi-physics method which makes the simultaneous investigation

of the aspects of high-Mach number flow, electrostatic and charge transport possible, were utilized to investigate the SIMHD generator in this study. COMSOL Multiphysics was used to model the present study. The results showed that the proposed SIMHD duct design increases the speed from 160 to 1300 m/s, while decreasing the temperature from 2100 to 1300 K. This can clearly have a positive effect on the performance and lifetime of the proposed generator. Moreover, the produced power for the resistive load 50 Ω equals 25.3 kW, which is a desirable and acceptable number. The present study also opens the venue for further research in this area. Future studies can work on the applicability of this generator in scramjets and ramjets since they make it possible to reach a speed of more than 1 Mach.

Ethical issue

The authors are aware of and comply with best practices in publication ethics, specifically with regard to authorship (avoidance of guest authorship), dual submission, manipulation of figures, competing interests, and compliance with policies on research ethics. The authors adhere to publication requirements that the submitted work is original and has not been published elsewhere.

Data availability statement

Datasets analyzed during the current study are available and can be given following a reasonable request from the corresponding author.

Conflict of interest

The authors declare no potential conflict of interest.

References

[1] V. A. Bityurin, C. A. Borghi, and P. L. Ribani, "High Enthalpy Extraction Numerical Experiment in a Plasma Vane MHD Generator," IEEE Trans. Plasma Sci., vol. 23, no. 5, pp. 844–851, 1995.

[2] H. Kobayashi and Y. Okuno, "Feasibility study on frozen inert gas plasma MHD generator," IEEE Trans. Plasma Sci., vol. 28, no. 4, pp. 1296–1302, 2000.

[3] S. P. Cicconardi and A. Perna, "Performance analysis of integrated systems based on MHD generators," Energy Procedia, vol. 45, pp. 1305–1314, 2014.

[4] N. Kayukawa, "Comparisons of MHD topping combined power generation systems," Energy Convers. Manag., vol. 41, no. 18, pp. 1953–1974, 2000.

[5] N. Kayukawa, "Open-cycle magnetohydrodynamic electrical power generation: A review and future perspectives," Prog. Energy Combust. Sci., vol. 30, no. 1, pp. 33–60, 2004.

[6] R. J. Rosa, "Scaling laws and the envelope of allowable operating conditions for an MHD generator using inert gases," Adv. Energy Convers., vol. 5, no. 4, pp. 265–277, 1965.

[7] J. Lineberry, B. Winklernan, and H. Schmidt, "Results of high power density MHD generator tests," Energy Convers. Eng. Conf. 1990. IECEC-90. Proc. 25th Intersoc., vol. 2, pp. 474–479, 1990.

[8] R. E. Voshall, R. J. Wright, and R. W. Liebermann, "Design of closed-cycle MHD generator with nonequilibrium ionization and system," IEEE Trans. Plasma Sci., vol. PS-5, no. 2, 1977.

[9] M. Tanaka, T. Murakami, and Y. Okuno, "Plasma characteristics and performance of magnetohydrodynamic generator with high-temperature inert gas plasma," IEEE Trans. Plasma Sci., vol. 42, no. 12, pp. 4020–4025, 2014.

[10] Y. Wang, X. Duan, P. Yan, H. Xue, and Q. Li, "A pulsed magnetohydrodynamic generator for electric launcher," IEEE Trans. Magn., vol. 41, no. 1 II, pp. 334–337, 2005.

[11] C. D. Sijoy and S. Chaturvedi, "Conversion of plasma energy into electrical pulse by magnetic flux compression," Fusion Eng. Des., vol. 86, no. 2–3, pp. 174–182, 2011.

[12] J. M. Wetzer, "Electron density determination in argon cesium MHD-plasmas," Physica, vol. 123, pp. 247–256, 1984.

[13] T. Murakami and T. Okamura, "Effect of Load Segmentation on the Performance of a Nonequilibrium Disk MHD Generator," IEEE Trans. Plasma Sci., vol. 30, no. 5, pp. 1999–2004, 2002.

[14] A. M. Howatson, An Introduction to Gas Discharges. Pergamon International Library of Science, Technology, Engineering and Social Studies, 2013.

[15] H. Kobayashi, Y. Okuno, and S. Kabashima, "Three-Dimensional Simulation of Nonequilibrium Seeded Plasma in Closed Cycle Disk MHD Generator," IEEE Trans. Plasma Sci., vol. 25, no. 2, pp. 380–385, 1997.

[16] V. R. Malghan, "History of MHD power plant development," Energy Convers. Manag., vol. 37, no. 5, pp. 569–590, 1996.

[17] D. E. Thomas, "Energy Conversion Alternatives Study-ECAS-: General Electric Phase I Final Report," US Government Printing Office, 1976.

[18] A. Montisci and R. Pintus, "Sensitivity analysis of design parameters of an inductive MHD generator," Power Electron. Electr. Drives Autom. Motion (SPEEDAM), 2010 Int. Symp., pp. 119–123, 2010.

[19] S. Carcangiu, A. Montisci, and R. Pintus, "Performance Analysis of an Inductive Mhd Generator," MAGNETOHYDRODYNAMIGS, vol. 48, no. 1, pp. 1–5, 2012.

[20] R. S. Delogu, M. Di Mauro, and A. Montisci, "Inquiry for the Technical Feasibility Assessment of a New Design of MHD Generator," in 13th Biennal IEEE Conference on Electromagnetic Field Computation (CEFC 2006), 2006.

[21] S. Carcangiu and A. Montisci, "Assessment of the machine parameters affecting the overall performance of an inductive MHD generator," Energy Conf. Exhib. (ENERGYCON), 2012 IEEE Int., pp. 271–275, 2012.

[22] R. Paciorri, W. Dieudonné, G. Degrez, J.-M. Charbonnier, and H. Deconinck, "Exploring the Validity of the Spalart-Allmaras Turbulence Model for Hypersonic Flows," J. Spacecr. Rockets, vol. 35, no. 2, pp. 121–126, 1998.

[23] R. Paciorri and F. Sabetta, "Compressibility Correction for the Spalart-Allmaras Model in Free-Shear Flows," J. Spacecr. Rockets, vol. 40, no. 3, pp. 326–331, 2003.

[24] D. R. Eklund and J. P. Drummondt, "Calculation of Supersonic Turbulent Reacting Coaxial Jets," vol. 28, no. 9, pp. 1633–1641, 1990.

[25] B. Aupoix and P. R. Spalart, “Extensions of the Spalart–Allmaras turbulence model to account for wall roughness,” Int. J. Heat Fluid Flow, vol. 24, no. 4, pp. 454–462, 2003.
[26] White, F. M., and I. Corfield. "Viscous Fluid Flow, vol. 3 McGraw-Hill." New York. (2006)
[27] Raizer, Yu P. "Gas discharge physics. Berlin: Springer-Verlag. 449 p." (1991) ISBN: 978-3-642-64760-4
[28] Castellanos, Antonio, ed. Electrohydrodynamics. Vol. 380. Springer Science & Business Media, 1998. https://doi.org/10.1007/978-3-7091-2522-9
[29] N. E. Jewell-larsen, S. V Karpov, I. a Krichtafovitch, V. Jayanty, C.-P. Hsu, and A. V Mamishev, “Modeling of corona-induced electrohydrodynamic flow with COMSOL multiphysics,” Proc. ESA Annu. Meet. Electrost., pp. 1–13, 2008.
[30] A. V Mikheev, N. Kayukawa, N. Okinaka, Y. Kamada, and S. Yatsu, “High-Temperature Coal-Syngas Plasma Characteristics for Advanced MHD Power Generation,” IEEE Trans. Energy Convers., vol. 21, no. 1, pp. 242–249, 2006.
[31] V. Nikonov, R. Bartnikas, and M. R. Wertheimer, “The influence of dielectric surface charge distribution upon the partial discharge behavior in short air gaps,” IEEE Trans. Plasma Sci., vol. 29, no. 6, pp. 866–874, 2001.
[32] M. R. Wertheimer, I. Radu, and R. Bartnikas, “Dielectric barrier discharges (DBD) in gases at atmospheric pressure: effect of charge trapping,” in Electrets, 2005. ISE-12. 2005 12th International Symposium on, 2005, no. 1, pp. 231–234.
[33] WALSH, EM. "Energy Conversion- Electromechanical, Direct, Nuclear (Book on electromechanical, direct and nuclear energy conversion covering transducer design, nuclear structure, photoelectric conversion, reactor theory, thermionic conversion, etc)." NEW YORK, RONALD PRESS CO., 1967. 408 P (1967) ISBN: 9780826091253